Available online at www.sciencedirect.com
SCIENCE DIRECT®
Journal of Nuclear Materials 347 (2005) 77–87
journal of nuclear materials
www.elsevier.com/locate/jnucmat

Colloids from the aqueous corrosion of uranium nuclear fuel

M.D. Kaminski *, N.M. Dimitrijevic, C.J. Mertz, M.M. Goldberg

Argonne National Laboratory, Chemical Engineering Division, 9700 South Cass Avenue, Argonne, IL 60439, USA

Received 3 March 2005; accepted 21 July 2005

Abstract

Colloids may enhance the subsurface transport of radionuclides and potentially compromise the long-term safe operation of the proposed radioactive waste repository at Yucca Mountain. Little data is available on colloid formation for the many different waste forms expected to be buried in the repository. This work expands the sparse database on colloids formed during the corrosion of metallic uranium nuclear fuel. We characterized spherical UO_2 and nickel-rich montmorilonite smectite-clay colloids formed during the corrosion of uranium metal fuel under bathtub conditions at 90 °C. Iron and chromium oxides and calcium carbonate colloids were present but were a minor population. The estimated upper concentration of the UO_2 and clays was 4×10^{11} and 7×10^{11}–3×10^{12} particles/L, respectively. However, oxygen eventually oxidized the UO_2 colloids, forming long filaments of weeksite $K_2(UO_2)_2Si_6O_{15} \cdot 4H_2O$ that settled from solution, reducing the UO_2 colloid population and leaving predominantly clay colloids. The smectite colloids were not affected by oxygen. Plutonium was not directly observed within the UO_2 colloids but partitioned completely to the colloid size fraction. The plutonium concentration in the colloidal fraction was slightly higher than the value used in the viability assessment model, and does not change in concentration with exposure to oxygen. This paper provides conclusive evidence for single-phase radioactive colloids composed of UO_2. However, its impact on repository safety is probably small since oxygen and silica availability will oxidize and effectively precipitate the UO_2 colloids from concentrated solutions.

PACS: 28.41.Kw

1. Introduction

A deep geologic repository under Yucca Mountain, Nevada, is the proposed site for the disposal of high-level waste and spent nuclear fuel in the US. To assess the safety of the repository, the DOE is developing predictive models that describe the time release of radioactivity. Radioactive colloids represent a potentially important component in the environmental transport of radioactivity from the repository. The formation of clay colloids during the alteration of high-level waste glass is well established [1,2] and recent studies describe the production of colloids that form during the corrosion of spent nuclear fuel [1,3,4]. However, the total system performance assessment [5], the governing scientific volume on the progress of the Yucca Mountain Site

* Corresponding author. Tel.: +1 630 252 4777; fax: +1 630 252 5246/4771.
E-mail address: kaminski@cmt.anl.gov (M.D. Kaminski).

0022-3115/$ - see front matter © 2005 Elsevier B.V. All rights reserved.
doi:10.1016/j.jnucmat.2005.07.009

Characterization Project, derives information on spent fuel colloids from limited data gathered from tests on commercial fuel that indicated very few colloids formed during corrosion. DOE-owned fuels, from research, test, and production reactors, have not been studied. At 2300 metric tons, metallic uranium nuclear fuel from the N-production reactors at Hanford comprises the vast majority of DOE-owned fuel and represents about 4% of the total spent fuel inventory slated for deep geological disposal. But, unlike commercial uranium dioxide fuel, uranium fuel corrodes very quickly, consuming dissolved oxygen, and creating oxide products with large surface areas [6] that facilitate surface reactions such as dissolution.

It is well established that uranium metal oxidizes quickly to UO_{2+x} in water [6]. However, colloid products associated with uranium corrosion in water have only recently been addressed in limited scope. These studies have included oxidative fuel corrosion under intermittent drips of well water [4], and under 'bathtub' conditions [7]. As part of a study on the corrosion of uranium fuel, we sought to expand the colloid database and identify any colloidal products that could form during the corrosion of uranium metal fuel in water. We chose to investigate, first, low oxygen conditions to simulate conditions where oxygen has been scavenged due to reaction with iron in the repository or reaction with the uranium fuel itself. Then, we studied the more probable scenario of oxygen being available for reaction and determined its effects on the colloids. The effect of sample aging was beyond the scope of this study. We describe the two predominant types of colloids formed – nickel-rich smectite clays and uranium dioxide – and their formation mechanisms. Oxygen dramatically reduced colloid numbers by precipitating uranyl silicates from solution. Plutonium partitioned strongly to the colloid phase and those values are compared to the Total System Performance Assessment modeling assumptions.

2. Methods and materials

2.1. Fuel and leachant

Both non-radiated and radiated fuel elements from the Hanford N-reactor (<1% burnup) were used. The actinide and fission product inventory for these fuels is low compared to commercial UO_2 fuels. Specimens were separated from the cladding and cut into small wedges (~100 mg). Then, they were polished to 600 grit with silicon carbide paper or powder and ultrasonically rinsed in deionized water.

The water leachant was either well water from the J-13 well (near Yucca Mountain) modified by reacting with the volcanic detritus called tuff that characterizes the Yucca Mountain strata as described elsewhere [3] or deionized water (>18 MΩ resistance). The modified well water (herein referred to as 'well water') simulated the water composition more likely to be encountered in the repository since the well water would have passed through many meters of tuff. It was rich in dissolved silica and other clay-forming elements (see Section 2.1 of [9]). The deionized water was used to examine the formation of UO_2 colloids without interference from well water-derived clay colloids (as will be described, clay colloids formed when the well water was reacted with the steel test vessel). This facilitated characterization of the UO_2 colloids by UV/VIS NIR, ζ-potential measurements, and laser light scattering.

2.2. Test configuration

The test configuration, called a 'bathtub' configuration, was initiated by placing the uranium fuel specimen at the bottom of a vessel, filling the vessel with water (14–16 mL/100 mg, $S/V = 0.023\ m^{-1}$), and heating the sealed vessel at 90 °C for up to 125 days. The vessel (30 mL cap.) was either 304 L stainless steel, high-density polyethylene (HDPE), or glass and was rinsed with 1% HNO_3 and deionized water prior to use. The steel vessel simulated corrosion within the fuel package while the HDPE and glass were used to avoid clay colloid formation.

The O_2 concentration in the water was either equilibrated with air (oxygenated) or purged with N_2 gas (oxygen starved, <0.1 μg/g or ppm O_2) for 10 min. The exact conditions for each test are shown in Table 1.

The vessel was maintained at 90 °C until sampled. To sample the test, the vessel was rapidly cooled to room temperature by contacting the vessel with dry ice, the cap was removed and small liquid (1.2 mL) or solid samples were withdrawn for analysis. The vessels were not cleaned prior to test continuation. Tests were continued after replenishing the water to the initial water volume in the vessel and heating the vessel to temperature.

A first set of tests (1a, 2a, and 5) was run under oxygen-starved conditions with non-radiated and radiated fuel specimens. However, oxygenated conditions are expected to dominate the chemistry of the repository (see page 3–68 of [5]). Therefore, we opened Test 1a and 2a to air after the anoxic period and monitored the resulting solution over time (Test 1b, 2b). The corrosion product produced in Test 5 was used for X-ray diffraction analysis. Several controls were included to account for the effect of the steel vessel on colloid formation with fuel present (Tests 3–4) and absent (Tests 6–8). The suite of controls facilitates the mechanistic understanding of the origin of colloids in our complex system.

2.3. Analysis

All analyses were carried out at room temperature.

Table 1
Test descriptions

Test number	Vessel type	Cold or hot fuel[a]	O_2	Duration (*d*)	Purpose	Analysis
1a	Steel[a]	Cold	None	115	Produce colloids under 'realistic' conditions, compare to radiated fuel	TEM, DLS
1b	Steel[a]	Cold	Air	61	Determine effect of air on colloids from solution in Test 1	TEM, DLS
2a	Steel	Hot	None	95	Produce colloids under 'realistic' conditions	Filtration, TEM, DLS
2b	Steel	Hot	Air	70	Determine effect of air on colloids from solution in Test 2	Filtration, DLS
3	HDPE	Hot	Air	56	Determine effect of O_2 and smectite-clay formation	Filtration, TEM, DLS
4	Glass[b]	Cold	None	50	Produce UO_2 colloids and no smectite clays	UV/VIS/IR, TEM, DLS, ζ-potential
5	Steel	Hot	None	125	Characterize uranium oxide product	XRD
6	Steel	None	None	151	Check contamination and growth of natural colloids	TEM, DLS
7	HDPE	None	Air	14	Check growth of natural colloids	TEM, DLS
8	Steel	None	Air	8	Check growth of natural colloids	TEM, DLS

[a] Cold and hot refer to non-radiated and radiated fuel, respectively.
[b] Deionized water used instead of modified J-13 well water.

2.3.1. Diffraction analysis

The powdered uranium-oxide corrosion product was removed from the steel vessel after 125 days (Test 5) and centrifuged to remove any liquid. A small amount of ethanol was added and the slurry was dripped onto a warm diffraction planchet ('zero-background' single crystal silicon) and dried rapidly. The dried sample was analyzed immediately by X-ray diffraction (Cu filament, 0.02°/step, 0.2°/min) and identified as UO_{2+x}. A silicon standard was used to check the instrument calibration. Peak fitting routines (Jade 5.0) were used to calculate the oxidation-state of the oxide product and crystallite size.

2.3.2. Photocorrelation spectroscopy

For similarly-sized colloids, light scattering intensity is directly proportional to colloid concentration. We screened unfiltered liquid samples for colloids by measuring the light scattering intensity at 90° (argon ion laser at 3 mW, 515 nm, 500 μm PMT aperture). Samples with intensities exceeding those for deionized water ($<5\times10^3$ cps) and modified well water stock ($<7\times10^3$ cps) were analyzed further. Large spurious light scattering intensities marked the presence of suspended material larger than colloidal dimensions. Samples displaying such spurious signals were centrifuged for 10 min (×7200*g*) and reanalyzed by light scattering. Latex standards were similarly centrifuged to confirm that true colloids remain in suspension, i.e., constant light scattering intensity. For example, the light scattering intensity of 100 nm diameter latex spheres remained constant after centrifugation while the scattering intensity for 300 nm latex spheres dropped by a factor of two.

We measured the temporal fluctuations in the scattering intensity over very short periods (<300 μs, Malvern 64 channel correlator) and analyzed the resulting correlation function with CONTIN [8] to obtain colloid size distributions. The size distribution was checked against polystyrene standards from Duke Scientific (32, 73, 304 nm diameters) and NIST (SRM 1963 and SRM 1691, 100 and 269 nm diameters, respectively) for agreement. Mean diameters are reported for all sample measurements and the standard deviation is calculated from the variance of the mean diameter measurements and not from the variance of individual measurements since the variance of individual sample measurements were large. Polystyrene colloid concentrations could be estimated based on the scattering intensity of known solutions as reported in [9]. Bimodal standards prepared from 32 to 100 nm standards confirmed our ability to de-convolute distinct colloid populations.

2.3.3. Electron microscopy

Transmission electron microscopy (accelerating voltage = 200 kV) characterized the morphology of colloids filtered through a film grid. Energy dispersive X-ray analysis and selected area electron diffraction provided micro-composition and *d*-spacing data, respectively. We prepared grids by passing unfiltered sample leachate through a hydrophobic formvar-coated grid (Ladd Research). The hydrophobicity of the grid is believed to cause significant sample artifacts by aggregating individual colloids heterogeneously across the grid. Our experiments with hydrophobic formvar and hydrophilic butvar grids (carbon grids modified in-house) showed the degree of aggregation experienced by gold colloids. However, it is unclear whether the butvar grids promote the antithesis by artificially dispersing colloids during sample preparation. Therefore, the microscopy method for determining the dimensions of colloid aggregates is

not reliable and we defer to light scattering for this information. There was no difference between colloids observed in radiated and non-radiated fuels.

2.3.4. Absorption spectrophotometry

Absorption spectra of liquid samples (Test 4) were recorded (UV–Vis-NIR double-beam spectrophotometer) to determine the bandgap energy of UO_2 colloids. First, 0.5 mL of solution was centrifuged to accelerate the effect of gravity and remove large precipitates greater than colloids. The supernatant was diluted with deionized water (1:1 volume) and the absorption spectra measured. The spectrum revealed two distinguishable features, one dominated by scattering, and another dominated by absorption. Resolving the two components gave the threshold wavelength λ which is a direct measure of the bandgap transition energy [10], ($E_g = \frac{hc}{\lambda}$). Deionized water was the reference sample.

2.3.5. Surface potential/charge/zeta-potential

The surface charge measured by the zeta-potential (ZetaPlus, Brookhaven Instruments Corp.) was performed in unfiltered aliquots adjusted in pH with $HClO_4$ or NaOH. The individual points represent mean values of at least five measurements. The zeta-potential values were measured in 10 mM $NaClO_4$ solution ($I = 0.01$ m).

2.3.6. Solution isotopic analysis

Quantitative partitioning of elements to the colloid and dissolved phases was measured by inductively coupled plasma-mass spectrometry (ICP-MS). Samples from Tests 2a and b were filtered sequentially through a 450 nm filter (Millipore-Ultrafree CL), and 30 kDa (<5 nm) filter to determine the fraction associated with colloidal material (5–450 nm) and dissolved species (<5 nm). Liquid samples were acidified to 1% HNO_3 prior to ICP-MS analysis.

3. Results

3.1. Colloids formed under anoxic corrosion

In oxygen-free well water, uranium corrodes to a fine black/brown oxide UO_{2+x} free of hydride (Fig. 1). The systematic shift in the X-ray diffraction lines corresponded to a cell parameter $a = 0.5462 \pm 0.0003$ nm (5.462 ± 0.003 Å). This compares to 0.5440 nm (5.440 Å) for U_4O_9 ($UO_{2.25}$) and 0.5468 nm (5.468 Å) for $UO_{2.03}$ suggesting a $UO_{2.08\pm0.03}$ product in agreement with the literature for corrosion in water-saturated oxygen-deprived conditions [6]. The severe line broadening corresponded to a very small crystallite size <10 nm, consistent with the dimensions of the spherical UO_2 colloids discussed shortly.

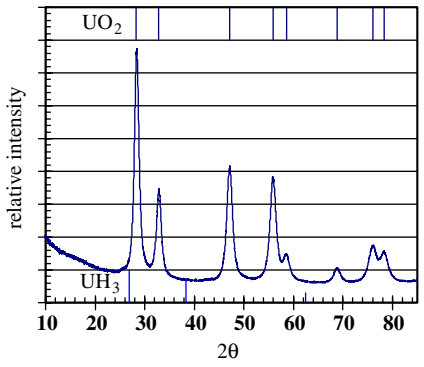

Fig. 1. X-ray diffraction pattern for UO_{2+x}. Note the peak positions for UO_2 (top vertical marks) and UH_3 (bottom vertical marks).

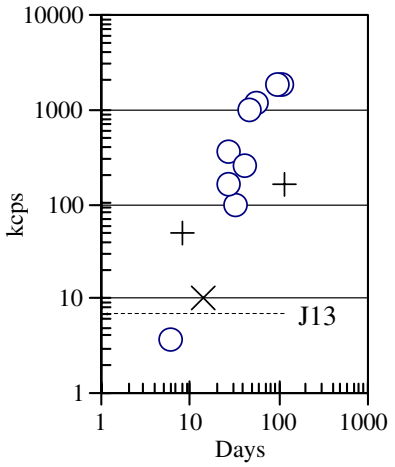

Fig. 2. Light scattering intensity as a function of test duration. (+) Indicates control test 6 and 8 in steel vessels. (×) Indicates control test 7 in HDPE vessel.

Light scattering intensities (Fig. 2) increased with test duration indicating a steady increase in the concentrations of colloids. Scattering intensities as high as 1850×10^3 counts/s (1850 kcps, polydispersity index PI > 0.3) greatly exceeded the background value of <7 kcps (well water stock solution). These high scattering intensities persisted after a month of storage and the large polydispersity index indicated broadly distributed colloid populations. Two major types of colloids were found (Fig. 3), uranium dioxide and clays, along with less prevalent colloids – Fe/Cr-rich colloids and Ca-rich colloids.

3.1.1. UO_2 colloids

The individual UO_2 spheres were primarily <10 nm in diameter (Fig. 3) but some were larger (100–150 nm). The individual spheres were found most often

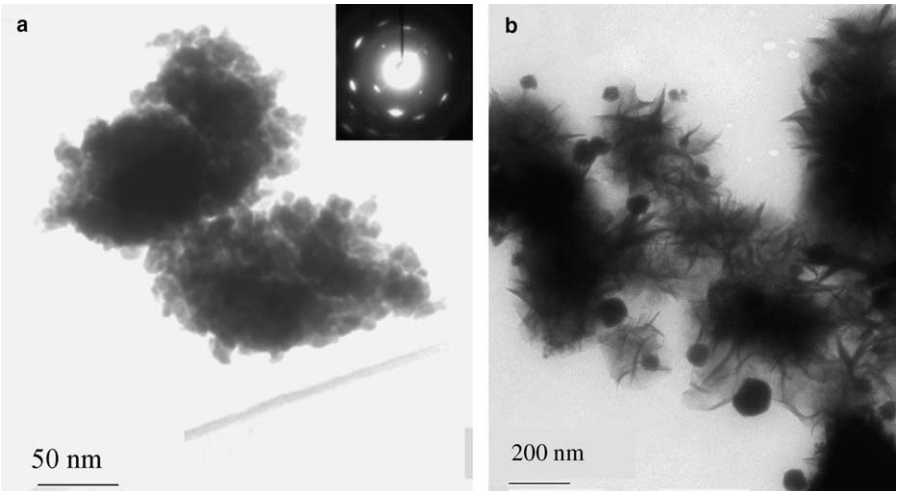

Fig. 3. Micrograph of (a) an agglomeration of UO_2 spheres (diffraction pattern shown in inset) and (b) nickel-rich smectite-clay colloids containing various diameter UO_2 spheres.

as agglomerates as large as 1000 nm, although most were less than 250 nm. Some isolated non-agglomerated spheres existed. Light scattering analysis of a solution containing only UO_2 colloids produced a mean size of 160 ± 60 nm (Test 4). Electron diffraction (inset in Fig. 3(a), Table 2) was consistent with sub-stoichiometric UO_2. UV/VIS (Fig. 4) of the UO_2 colloids provided a bandgap energy of 2.98 eV (threshold wavelength $\lambda = 417$ nm) and the zeta-potential was pH 2–3 (Fig. 5).

3.1.2. Smectite-clay colloids

Ubiquitous in samples containing both well water and steel were nickel-rich layered silicate clays similar in morphology to the smectite-clays described by Buck and Bates [2]. The smectite clays (Fig. 3(b)) contained Si, Ni, Fe, and Al to varying degrees according to X-ray analysis. Electron diffraction analysis of morphologically similar colloids generated in Test 8 produced *d*-spacings (Table 2) consistent with montmorilonite smectite-type clay. Unfortunately, the clay colloids were too thin to provide a high-quality electron diffraction pattern so we have no further evidence to assign these colloids as smectite clays. The clays ranged in size from

Table 2
Diffraction data for UO_2 and smectite-clay colloids

UO_2		Montmorilonite smectite	
Test 1a	ICDD index	Test 8	ICDD index
3.22 ± 0.04	3.155	2.47	2.56
2.63 ± 0.03	2.733	1.47	1.495
1.95 ± 0.02	1.933		
1.68 ± 0.01	1.680		
1.54 ± 0.01	1.578		

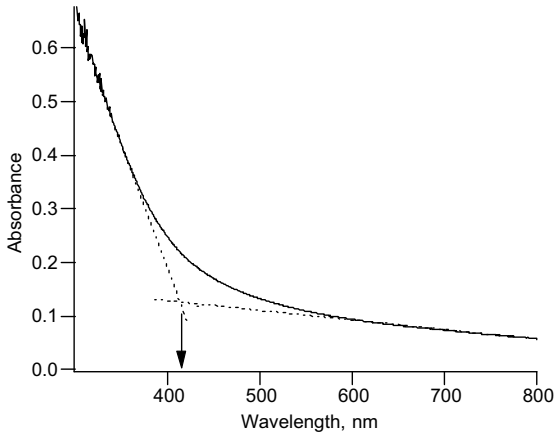

Fig. 4. Threshold wavelength for UO_{2+x} colloids was 417 nm.

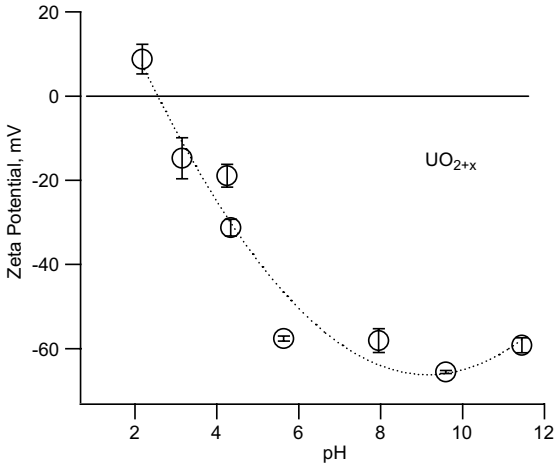

Fig. 5. Zeta-potential of UO_{2+x}.

100 to >1000 nm as evidenced by microscopy. The mean diameter determined by light scattering of the mixed colloids (clays and UO_2 colloids) formed in the steel vessel (Tests 1a and 2a) was 260 ± 60 nm ($n = 15$) suggesting that the mean diameter of clay colloids was larger than 260 nm since the mean size of UO_2 colloids was 160 ± 60 nm. We found the UO_2 spheres often imbedded within the smectite phase assemblage (Fig. 3(b)) although it is difficult to determine whether this is an artifact of a hydrophobic sample material or a realistic representation of colloidal aggregation in the test solution.

3.1.3. Other colloids

Other less common types of colloids were aggregates rich in iron and chromium, and those rich in calcium (not shown). No other elements were detected with calcium by X-ray analysis.

3.2. Effect of oxygen on colloids

When the fuel reacted in air (Test 3), the light scattering intensity was large but erratic (480–720 kcps) indicating suspended material larger than colloid dimensions. The intensity dropped to background levels (4 kcps) after centrifuging. X-ray analysis and electron diffraction showed that the suspended material was filamentous crystals of weeksite $K_2(UO_2)_2Si_6O_{15}\cdot 4H_2O$ (Fig. 6).

Oxygen appeared to have no effect on the nucleation of the Fe/Cr-rich and calcium-rich colloids.

3.3. Colloid-associated radionuclide concentrations

3.3.1. Oxygen-starved conditions

The concentration of uranium (Fig. 7) and plutonium in the colloid phase increased steadily during the corrosion of the metal in the absence of oxygen. At its highest concentration, the colloid fraction was 3.8×10^{-5} M (9100 ng/g or ppb) uranium as opposed to a dissolved concentration of 4.2×10^{-6} M (1000 ppb). Plutonium, constituting <0.2% of the burned fuel mass, partitioned nearly quantitatively to the colloidal fraction at 1.6×10^{-8} M (3.9 ppb), 1.3×10^{-7} M (30.6 ppb), and 1.7×10^{-7} M (41 ppb) after 28, 41, and 95 days, respectively. The Pu/U ratios in the colloidal fraction were 0.010 ± 0.005 and 0.0045 ± 0.008 for 41 and 95 days, respectively. These values are much greater than the pre-corroded fuel matrix ratio of 0.002. Only one sample contained dissolved Pu in detectable concentrations (Pu = 2×10^{-9} M at 41 days).

Neptunium concentrations were below the detection limits of 8.4×10^{-10} M (0.2 ppb).

3.3.2. Oxygenated conditions

When oxygen was made available to a previously anoxic test solution, the uranium concentrations (Test 2b) associated with the colloids decreased steadily to 9.7×10^{-6} M (2300 ppb) from 3.8×10^{-5} M (9100 ppb) after 70 days; the dissolved fraction increased from 3.8×10^{-6} M (900 ppb) to 1.9×10^{-5} M (4500 ppb) during this time. Light scattering intensities reflected a

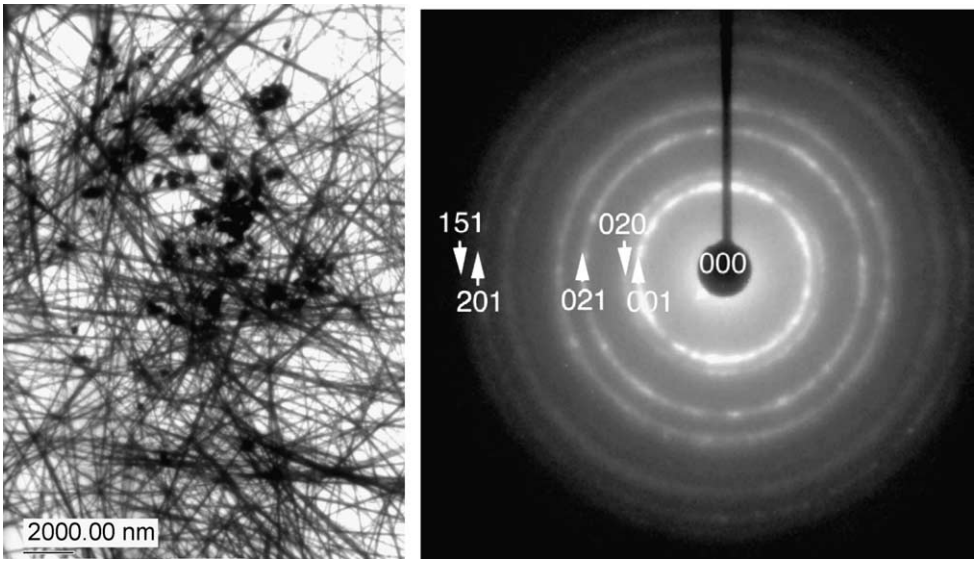

Fig. 6. Filaments of weeksite and UO_2 spheres (electron diffraction of weeksite shown to the right). The agglomerated UO_2 spheres could be seen attached to these filaments.

similar decrease in colloid concentration, showing a decrease from 1800 kcps to 270 kcps after 45 days and 350 kcps after 70 days exposed to oxygen. This intensity is greater than observed for the blank that produced clays, Fe/Cr-rich, and calcium (carbonate) colloids suggesting that the UO_2 colloids persisted after 70 days, which agrees with the filtration colloid data.

Plutonium remained partitioned quantitatively to the colloid fraction. The measured concentrations were 1.7×10^{-7} M (41 ppb), 2.3×10^{-7} M (55 ppb), and 1.1×10^{-7} M (26 ppb) for 0, 35, and 70 days exposed to air, respectively. The Pu/U ratios in the colloidal fraction were similar to oxygen-starved conditions, being, 0.012 ± 0.005 and 0.011 ± 0.005 at 35 and 70 days, respectively. Neptunium was below detection limits.

Analysis of filtrates from Test 3 confirmed the partitioning of uranium mostly to large particulate ($85 \pm 7\%$) as opposed to the colloid ($8 \pm 1\%$) and dissolved ($4.5 \pm 0.3\%$) fractions, consistent with the observed precipitation of weeksite and persistence of UO_2 colloids. The total uranium in solution was 9.5×10^{-5} M (22 500 ppb). Plutonium, partitioned to the colloid phase ($58 \pm 35\%$) and large particulate ($40 \pm 40\%$), indicated incorporation within the weeksite crystals. The total plutonium found in solution was 1.5×10^{-7} M (35.4 ppb). Neptunium was found in the large particulate ($60 \pm 38\%$) and in the dissolved fraction ($27 \pm 9\%$) with possibly some in the colloids ($16 \pm 28\%$). The total neptunium found in solution was 1.6×10^{-9} M (0.37 ppb).

With microscopy, we identified nickel-rich smectite clays and Fe/Cr-rich colloids and their persistence during these tests.

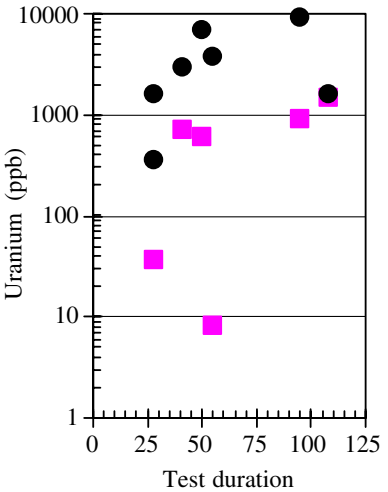

Fig. 7. Colloid (circles) and dissolved fractions (squares) for uranium.

3.4. Maximum colloid concentrations

3.4.1. UO_2 colloids

Two methods were available to estimate colloid concentrations in our laboratory. The first method [9] compares light scattering intensities to known concentrations of latex nanospheres of similar diameter. This method works well for refractive indices that are closely matched between unknown and standard but can be inaccurate for unmatched refractive indices [11]. The refractive index for UO_2 ($n_{RI} = 2.4$ [12]) is different than latex ($n_{RI} = 1.53$–1.64) so this method of calculation would represent an upper limit. However, the scattering intensity is proportional to the particle refractive index, so we can divide the scattering intensity of the UO_2 colloids by the ratio $n_{RI}^{UO_2}/n_{RI}^{PS} = 1.5$ to obtain an equivalent polystyrene scattering intensity. Then, Fig. 8 can be used with confidence. Since we do not have laser light scattering intensities of UO_2 colloids alone we must estimate its values from combined UO_2 and clay colloid scattering intensities. A maximum scattering intensity of 1850 kcps is conservative. Based on microscopy, we observed roughly equal proportions of UO_2 aggregates and clay colloids. So, if the UO_2 and clays scattered light identically (i.e., identical refractive indices, size, and shape), the scattering intensity for the UO_2 colloids would be approximately one-half 1850 kcps or 925 kcps. But, the refractive indices are different and the size is different. We assume the differences in shape can be ignored (see Section 3.4.2 for in depth explanation). We can account for these differences by invoking $n_{RI}^{UO_2}/n_{RI}^{PS} = 1.5$ and the sixth power relationship between size and scattering intensity

$$\frac{I_{160\,nm}}{I_{200\,nm}} = \frac{(80)^6}{(100)^6} = 0.262. \tag{1}$$

Combining this value with the refractive index we arrive at the relationship

$$\frac{I_{UO_2}}{I_{clay}} = 0.4. \tag{2}$$

Then,

$$\begin{aligned} &I_{clay} + I_{UO_2} = 1850, \\ &I_{clay} + 0.4 I_{clay} = 1850, \\ &I_{clay} = 1320, \\ &I_{UO_2} = 530. \end{aligned} \tag{3}$$

By employing this technique and assuming a colloid diameter of 300 nm,[1] a maximum UO_2 colloid concentration of 2×10^{11} particles/L was derived. For 100 nm colloids, the estimated maximum UO_2 colloid

[1] We are forced to correlate with 100 and 269 or 300 nm spheres because 160 nm spheres are not available for analysis.

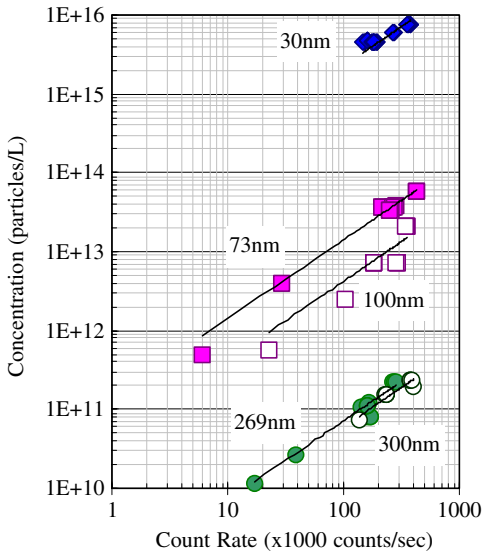

Fig. 8. Standard plots used to estimate colloid concentrations. (Trend continues to at least 1800 kcps. Data points greater than 500 kcps not shown.)

concentration was 2×10^{13} particles/L. By performing a linear interpolation [9] between the particle concentration and log of the radius to the sixth power, we arrive at a concentration of 3×10^{12} particles/L with 160 nm diameter.

Another method is by simple geometric calculations. We assumed the colloids were composed of spherical agglomerates of UO_2 with diameters matching the light scattering data[2] of $D = 160$ nm and maximum uranium concentration consistent with the data in Fig. 5 (9100 ppb). Each spherical agglomerate has a mass of $(4/3)\pi\rho(D/2)^3 = 5.8 \times 10^{-12}$ ng/particle with diameter D in nm and density ρ equal to 11 g/cm^3 and a packing fraction of 0.7. We can calculate the particle density

$$\frac{9100\ \left[\frac{\text{ng}}{\text{g}}\right] \times 10^3\ \left[\frac{\text{g}}{\text{L}}\right] \times \left(\frac{238+32}{238}\right)\ \frac{\text{gUO}_2}{\text{gU}}}{(4/3)\pi\rho(D/2)^3 \times 10^{-12}\ \left[\frac{\text{cm}^3}{\text{nm}^3}\ \frac{\text{ng}}{\text{g}}\right] \times 0.7} = 7 \times 10^{11}\ \text{particles/L}. \quad (4)$$

If we assume $D = 10$ nm, consistent with the TEM observations of the individual UO_2 spheres, then the concentration of individual spheres was 2×10^{15} particles/L.

3.4.2. Clay colloids

To determine the clay colloid concentrations, we assume that the majority of colloids generated in the blank Test 8 were clays (good assumption based on microscopy). The refractive index for clays ($n_{RI} = 1.6$) matches well with latex but it is apparent from microscopy that the morphology of the clay aggregates was not spherical (Fig. 2(b)) but more circular or similar to a flat, square cylinder. From [11], the hydrodynamic radius and radius of gyration for a sphere is r and $\sqrt{\frac{3}{2}}r$, respectively. The same values for a flat, square cylinder are $\frac{3}{2}r$ and $\sqrt{\frac{1}{2}}r$, respectively. Since these values are within the errors associated with our methods of estimating the colloid concentration, we ignore them with negligible consequence. The light scattering intensity (160 kcps) corresponded to 1×10^{11} particles/L assuming the clays are 300 nm average diameter or 6×10^{12} at 100 nm. A separate experiment conducted in steel vessels with well water exposed to air produced an average clay size of 200 nm. The concentration of 200 nm colloids is 4×10^{11} particles/L using the same interpolation method described above.

4. Discussion

There is a deficit in data on the occurrence of different types of colloids formed during the corrosion of nuclear fuel, especially those carrying radioactivity. Pertinent colloid information includes type, concentration, mechanism of formation, radioactivity loading, and stability.

The type of colloids formed within a particular test depends on the available reactants (Table 3). Since glass,[3] HDPE, and deionized water do not provide unique reactants for corrosion or formation of colloidal products, the reactants considered include uranium fuel, steel from the vessel (providing iron, chromium, and nickel), dissolved components in the well water, and O_2. Aqueous corrosion of uranium fuel under bathtub conditions produces copious colloids of both uranium-rich spheres and nickel-rich montmorilonite clays. It is clear from microscopy that UO_2 colloids form regardless of whether well water or deionized water is used. It is also clear from microscopy that both the steel and well water are needed to produce clay colloids. The Fe/Cr oxide and calcium colloids also appear to require both steel and well water. Iron oxyhydroxides are common natural colloids and we conjecture that Cr(III) may replace ferric ions in the colloid thus explaining the presence of chromium. In addition, colloids rich in calcium are formed. These are probably calcium carbonates, since no other elements were detected. But, when the test vessel was HDPE (Test 7) the well water does not foster colloid nucleation (light scattering intensity = 10 kcps)

[2] We use 160 nm from Test 2 instead of 260 nm from Test 1 because Test 2 solution analysis did not contain interference from clay colloids.

[3] Silica leached from the Pyrex glass is expected to be minimal during the test period due to the silica-saturated conditions of the well water.

Table 3
Reactants and colloid products (as identified by transmission electron microscopy)

Reactants present				Colloid products observed				
U	Steel	J-13[a]	O_2	Clays	UO_2	Fe/Cr	Ca	Weeksite
X	X	X		X	X	X	X	–
X	X	X	X	X	X	X	X	X
X		[b]		–	X	–	–	–
	X	X		X	–	X	X	–
	X	X	X	X	–	X	X	–
	[c]	X		–	–	–	–	–

Weeksite is shown to highlight effect of O_2 although the weeksite crystals settled out of solution as a precipitate.
[a] Well water.
[b] Reacted in deionized water.
[c] Reacted in an HDPE bottle.

significantly greater than the background value. Oxygen affects only the UO_2 colloids, causing the partial oxidation, dissolution, and subsequent precipitation of weeksite crystals.

4.1. UO_2 colloids

Initially, and regardless of oxygen concentration, the uranium-rich colloids are UO_2. Electron diffraction and energy dispersive X-ray analysis indicate such. The measured point of zero-charge (pH = 2–3) is consistent with literature values (3.0 for natural uraninite [13] and uranium rich ore [14]) and the bandgap energy of 2.98 eV corresponds well to the literature values for mono-crystalline UO_2 (2.90–3.05 eV) [15]. X-ray diffraction confirmed the formation of colloid-size crystallites <10 nm consistent with the diameter of individual UO_2 spheres (Fig. 2(a)) suggesting that a spallation mechanism describes UO_2 colloid formation. This mechanism differs from the redox precipitation of uranyl ions described recently by O'Loughlin [16]. Agglomerations appear to be common and diameters widely vary but are predominantly <250 nm, as indicated by microscopy and light scattering. However, there is evidence that a colloid population with diameter <10 nm may exist with concentrations up to 2×10^{15} particles/L.

The mechanism of formation of the UO_2 colloids is consistent with spallation directly from the fuel surface. A similar mechanism was reported by Buck and Bates [2] as an explanation for the smectite-clay colloids formed during the corrosion of high-level waste glasses. Spallation arises due to the excessive strain energies developed within the lattice from the disparity in densities between the metal substrate ($\rho = \sim 19$ g/cm^3) and the oxide film ($\rho = \sim 11$ g/cm^3). As further evidence, the steady increase in colloidal uranium concentration (Fig. 2) points to spallation since the amount of spalled colloids should be, then, directly related to the amount of corrosion (oxidation). If solubility limits for UO_2 had been reached, then a threshold concentration of dissolved uranium should have been reached prior to colloid formation. This is not the case as colloids are found immediately and increases with test duration as the dissolved uranium concentration increase during the anoxic period.

The spallation of UO_2 colloids is significant because, as the data shows the UO_2 colloidal products will form regardless of the presence of oxygen. That is, the UO_2 colloids will form first in the paragenetic sequence. Oxygen promotes a decrease in colloidal uranium while the dissolved component increases as uranyl species are formed. Microscopy and light scattering illustrate the near elimination of suspended colloidal material in oxygenated water and the precipitation of filaments of weeksite consistent with silica-rich natural systems [17].

The concentration of UO_2 colloids was dependent on the availability of oxygen. When oxygen is absent, the UO_2 colloid concentration is 7×10^{11} particles/L from geometric calculations. This value matches reasonably well the peak number 3×10^{12} particles/L calculated based on light scattering intensities. The presence of oxygen will eventually reduce the UO_2 colloid concentration to less than unreacted well water concentrations of 10^{10} particles/L although this drop is not instantaneous. It is interesting to consider whether stable populations of individual, dispersed UO_2 colloids exist in solution in addition to the 160 nm aggregates. Microscopy clearly supports the possibility and Mertz et al. [7] reported laser light scattering data that described a bimodal uranium colloid distribution with mean values of 4 ± 1 and 145 ± 22 nm. It certainly is possible that the 4 nm colloid component was below detection limits set by the dramatically more efficient scatterers making up the larger 160 nm component. Indeed, the scattering intensity ratios $I_{10\,nm}/I_{160\,nm} = 2 \times 10^7$ provide theoretical basis. We estimate the detection limits for our 10 nm UO_2 colloids by assuming that a peak height of <10% cannot be resolved by our photocorrelation spectrometer and calculate the intensity ratio based on peak area, peak area = 38 (10% of 380 = 38 kcps). This

intensity and Fig. 8 indicate a detection limit of 9×10^{14} particles/L for 30 nm colloids or 7×10^{17} particles/L for 10 nm colloids, making it impossible for light scattering at 3 mW to detect these concentrations. The peak values for 160 nm colloidal aggregates are two orders of magnitude higher than the concentration of natural colloids incoming to the repository (see page 3–73 of [5]). The peak values for 10 nm colloids are seven orders of magnitude higher than natural colloids.

4.2. Plutonium disposition

Plutonium is unequivocally partitioned to the colloidal fraction and not affected by oxygen during the study period, although its exact disposition (i.e., distinct Pu colloid phases or sorbed to clays) could not be identified. The enrichment of plutonium compared to uranium in the colloids strongly suggests that the two elements follow different reactive paths, which we will explain. First, we expect plutonium to be incorporated in the UO_2 colloids during the solid-state oxidation of the metal if the release of Pu and U is congruent. Thus, the concentration within UO_2 colloids is expected to correlate with the Pu/U ratios in burned fuel (0.2%) or $9100\ \text{ppb} \times 0.002 = 18.2$ ppb Pu in the UO_2 lattice. We would also expect the congruent release of plutonium when uranium dissolves. With 1000 ppb uranium dissolved in solution, we expect $1000 \times 0.002 = 2$ ppb Pu released to solution to remain dissolved or available to react further. The calculated total of 20 ppb plutonium is much less than the 41 ppb found in solution. Thus, we must conclude that congruent release of plutonium from the fuel is inaccurate, an observation consistent with that of [18]. However, we still cannot account for the disposition of plutonium – where is half of it? Plutonium can strongly sorb to clays but current understanding and models [19] require an equilibrium between soluble and sorbed plutonium species. As we did not find any soluble plutonium, and partitioning coefficients measured for plutonium on clays is not sufficiently high [19], clays cannot account for plutonium sorption to clay surfaces. Thus, we are left to consider discrete plutonium colloids existing as plutonium polymers [20] as described in the Yucca Mountain modeling reports [19]. Since little is known about the stability of plutonium polymers we cannot support or refute its existence. We measured plutonium colloid concentrations of 1.6×10^{-8}–1.7×10^{-7} M, the highest value being slightly higher than the TSPA value of 8×10^{-8} M ($I < 0.01$ m) [19].

4.3. Neptunium disposition

Neptunium could not be determined with accuracy in the colloid phase although the total concentration is low in the uranium fuel compared to other fuels expected in the repository.

4.4. Clay colloids

A common feature for the colloids formed in the steel vessel with well water is the persistence of nickel-rich montmorilonite smectite clays. Clays were a common feature in the corrosion of borosilicate glass [2] and uranium–aluminum intermetallic fuels [9], but the prevalence of nickel in the smectite clays is unique to this system presumably due to direct contact between the steel vessels and the fuel during oxidation. The maximum concentration of nickel-rich smectite colloids is estimated to be 4×10^{11} particles/L and was not affected by oxygen. The presence of nickel in the smectite clays found here suggests that the corrosion of the steel vessel was an integral part of the mechanism of their formation. The participation of steel components is also suggested by the lack of colloids in tests run with HDPE (Fig. 2).

5. Conclusion

We expanded the breadth of knowledge on the colloids formed from one particular fuel expected for disposal in the repository. The UO_2 colloids are the first conclusive evidence for single-phase radioactive colloids that has been reported in the literature. The work by Finn et al. [18] suggested that uranyl-type colloids may exist after corrosion of commercial UO_2 fuel but the evidence was very sparse, finding only one such particle during their microscopic examination. The data in Finn et al. [18] suggest, instead, that the uranyl-type colloid that was reported may be as likely an experimental artifact as evidence for colloids. Our results show that UO_2 colloids are the primary paragenetic outcome during the initial corrosion phase of uranium fuel, but, if oxygen is provided to the system, as the TSPA models predicts, then the uranyl silicates will precipitate from solution and greatly reduce or eventually eliminate the UO_2 colloid population.

Acknowledgements

The authors thank J. Holly and J. Fortner for assistance with TEM analysis, Y. Tsai and S. Wolf for ICP-MS analysis, J. Emery and M. Clark for test setup and fabrication, C. Shelton-Davis for useful discussion and program support, and V. Strezo and S. Zussman for helpful editing and document preparation. This work was supported by the National Spent Nuclear Fuel Program Release Rate Program and the US Department of Energy, under contract W-31-109-ENG-38.

The submitted manuscript has been created by the University of Chicago as Operator of Argonne National Laboratory ('Argonne') under Contract No. W-31-109-

References

[1] H. Geckeis, B. Grambow, A. Loida, B. Luckscheiter, E. Smailos, J. Quinones, J Radiochim Acta 82 (1998) 123.
[2] E.C. Buck, J.K. Bates, Appl. Geochem. 14 (1999) 635.
[3] M.D. Kaminski, M.M. Goldberg, J. Nucl. Mater. 304 (2002) 182.
[4] J.A. Fortner, C.J. Mertz, M.M. Goldberg, C.V. Shelton-Davis, Corrosive alteration of N-reactor fuel exposed to unsaturated conditions using simulated groundwater, in: 9th International High-Level Radioactive Waste Management Conference, Las Vegas, NV, April 29–May 3 2001.
[5] US Department Of Energy, Office of Civilian Radioactive Waste Management, DOE/RW-0508/V3 (1998).
[6] C.A. Colmenares, Prog. Solid State Chem. 15 (1984) 257.
[7] C.J. Mertz, J.A. Fortner, M.M. Goldberg, C.V. Shelton-Davis, in: Presented at the TMS 2000 Fall Meeting, St. Louis, Missouri, 8–12 October 2000.
[8] S.W. Provencher, Comput. Phys. Commun. 27 (1982) 213.
[9] M.D. Kaminski, M.M. Goldberg, C.J. Mertz, J. Nucl. Mater., this issue, doi:10.1016/j.jnucmat.2005.07.010.
[10] J.I. Pankove, Optical Properties in Semiconductors, Prentice-Hall, New Jersey, 1971.
[11] P. Schurtenberger, M.E. Newman, in: Environmental Particles, Environmental Analytical and Physical Chemistry Series, Vol. 2, Lewis Publishers, Ann Arbor, 1993, p. 95.
[12] W.D. Wilkinson, Uranium Metallurgy, Uranium Corrosion and Alloys, Vol. II, Interscience Publishers, New York, 1962.
[13] H.C. Parreira, R.H. Ottewill, An. di Acad. Brasileira de Ciencias 32 (1960) 35.
[14] J.S. Laskowski, J. Ralston (Eds.), Colloid Chemistry in Mineral Processing, Elsevier, New York, 1992, 270.
[15] J.J. Schoenes, Chem. Soc., Faraday Trans. 2 (83) (1987) 1205.
[16] E.J. O'Loughlin, S.D. Kelly, R.E. Cook, R. Csencsits, K.M. Kemner, Environ. Sci. Technol. 37 (4) (2003) 721.
[17] Systematics and paragenesis of uranium minerals, in: P.C. Burns, R. Finch (Eds.), Uranium: Mineralogy, Geochemistry and the Environment, Reviews in Mineralogy, Vol. 38, 1999.
[18] P.A. Finn, E.C. Buck, M. Gong, J.C. Hoh, J.W. Emery, L.D. Hafenrichter, J.K. Bates, Radiochim Acta 66/67 (1994) 189.
[19] CRWMS M&O. Waste Form Colloid-Associated Concentrations Limits: Abstraction and Summary. ANL-WIS-MD000012 Rev 00ICN01, Las Vegas, NV: CRWMS M&O, Dec. 2000.
[20] G.L. Silver, J. Radioanal. Nucl. Chem. 247 (3) (2001) 561.